Optics Communications 328 (2014) 135–142

Contents lists available at ScienceDirect

Optics Communications

journal homepage: www.elsevier.com/locate/optcom

Infrared to terahertz absorption window in mono- and multi-layer graphene systems

Y.M. Xiao [a], W. Xu [a,b,*], F.M. Peeters [c]

[a] Department of Physics, Yunnan University, Kunming 650091, China
[b] Key Laboratory of Materials Physics, Institute of Solid State Physics, Chinese Academy of Sciences, Hefei 230031, China
[c] Department of Physics, University of Antwerp, Groenenborgerlaan 171, B-2020 Antwerpen, Belgium

ARTICLE INFO

Article history:
Received 18 January 2014
Received in revised form
18 April 2014
Accepted 28 April 2014
Available online 13 May 2014

Keywords:
Graphene
AB-stacking
ABC-stacking
Light transmittance
Optical conductance

ABSTRACT

We present a theoretical study on optical properties such as optical conductance and light transmission coefficient for mono- and multi-layer graphene systems with AB- and ABC-stacking. Considering an air/graphene/dielectric-wafer structure, the optical coefficients for those graphene systems are examined and compared. The universal optical conductance $\sigma_0^N = N\pi e^2/(2h)$ for N layer graphene systems in the visible region is verified. For $N \geq 3$ layer graphene, the mini-gap induced absorption edges can be observed in odd layers AB-stacked multilayer graphene, where the number and position of the absorption edges are decided by the layers number N. Meanwhile, we can observe the optical absorption windows for those graphene systems in the infrared to terahertz bandwidth (0.2–150 THz). The absorption window is induced by different transition energies required for inter- and intra-band optical absorption channels. We find that the depth and width of the absorption window can be tuned not only via varying temperature and electron density but also by changing the number of graphene layers and the stacking order. These theoretical findings demonstrate that mono- and multi-layer graphene systems can be applied as frequency tunable optoelectronic devices working in infrared to terahertz bandwidth.

1. Introduction

Since the breakthrough discovery of graphene in 2004 [1], the investigation into graphene based novel devices has become a fast-growing field of research due to their extremely useful physical properties, including very high electron mobility, high mechanical strength, excellent thermal conductivity, optoelectronic properties, etc. At present, transparent flexible electronics on the basis of graphene devices is a much sought technology with important applications that can range from foldable displays and electronic paper, to transparent solar cells. It has been found that an air/graphene/dielectric-wafer system has high light transmittance from UV to near-infrared bandwidth. This makes it possible to replace the conventional indium tin oxide (ITO) transparent electrodes [2,3] in producing better and cheaper LED, LCD, etc. The variable optical transmittance in graphene systems can make a new breed of optical modulators with broad optical and electrical bandwidths [4–6]. Meanwhile, graphene based photodetectors have also received considerable attention because of the broad spectral bandwidth and ultrafast response time [7–9]. It has been shown that graphene is an intrinsically two-dimensional (2D) material with sensitive electrostatic perturbation conductance induced by photo-generated carriers close to the surface which makes graphene a particularly promising material for high gain photo-detection by employing the photo-gating effect [10]. Moreover, graphene has been considered as a promising candidate for photosensitive terahertz (10^{12} Hz or THz) devices, due to its gapless density of states and high quantum efficiency. It has been demonstrated experimentally that the optical conductivity of graphene in THz regime can be well described by the Drude model, implying that graphene is a metallic like THz material [11]. In addition, the strong nonlinear optical response in mono- and bi-layer graphene systems from THz to far-infrared regime makes graphene a preferred material for nonlinear photonics and optoelectronics devices [12,13].

It is known that mono- and bi-layer graphene systems are gapless 2D electronic structures, whereas the ABC-stacked tri-layer graphene becomes a semiconductor with tunable fundamental band gap. For multilayer graphene films, the electronic structures depend strongly on layers number and stacking order. Thus, the features of electronic band structure can directly affect the electronic and optical properties of graphene systems with different graphene layers. At present, the low-cost and reliable growth of high quality and large size graphene films are mainly

* Corresponding author at: Department of Physics, Yunnan University, Kunming 650091, China.
E-mail address: wenxu_issp@aliyun.com (W. Xu).

http://dx.doi.org/10.1016/j.optcom.2014.04.079
0030-4018/

based on a chemical vapor deposition (CVD) technique [14]. Multilayer graphene samples are the main products of the CVD growth. In recent years, the optical and optoelectronic properties of different graphene systems have been investigated intensively. Theoretically, the electronic band structures for systems with different graphene layers have been examined [15–17,27–29]. The low-temperature optical conductivity for both monolayer and AB-stacked multilayer graphene was calculated using the Kubo formula [18], where optical properties for different graphene systems were examined in UV to far-infrared regime. Experimentally, the optical properties of epitaxial graphene from visible to THz range were measured and the high transmittance windows were observed in infrared and THz regime for multilayer graphene systems [19]. It has been found that the optical conductance per graphene layer is a universal value $\sigma_0=\pi e^2/(2h)$ in visible bandwidth [20,21]. The corresponding light transmittances for mono-, bi- and tri-layer graphene are about 97.7%, 95.4% and 93.1%, respectively, and the opacity is about 2.3% per graphene layer [22]. Furthermore, it has been observed that there exists an optical absorption window in mono-layer graphene at room-temperature [20,21] in the mid-infrared to THz regime. The width and depth of this absorption window in monolayer graphene depend strongly on temperature and carrier density, especially at the lower frequency edge. These findings imply that graphene systems can be applied for infrared or THz detection in ambient condition. Our previous theoretical work [23] shown that the THz absorption window can also be achieved in bilayer graphene systems.

Currently, the major results for optical properties of mono- and bi-layer graphene systems have been well documented. However, less research work has been conducted for graphene systems with layer number $N\geq 3$. Most theoretical work on optical properties of multi-layer graphene has been focused mainly on ultraviolet to infrared absorption peaks and universal optical conductance observed in visual light regime [18]. In this paper, we employ the effective low-energy model to study the responses of mono- and multi-layer graphene systems to the radiation field. It is known qualitatively that in infrared to THz region, the number of graphene layers must have influence on optical properties of the graphene systems. It is of great importance and significance to provide a quantitative answer about how optoelectronic properties of mono- and multi-layer graphene systems vary with the number of graphene layers and with the stacking orders. This becomes a prime motivation of the present theoretical study.

2. Theoretical approaches

We consider that a graphene sheet is placed on the xy-plane on top of a dielectric wafer such as SiO_2 substrate and a weak radiation field is applied with linear polarization along the x-direction. The vector potential of the light field is $A(t)=F_0\sin(2\pi\nu t)/(2\pi\nu)$, where F_0 and ν are the electric field strength and the frequency of the light field, respectively. The optoelectronic response of the graphene system in such a situation can be studied through the balance equation approach [24] derived from the semiclassical Boltzmann equation. With this approach, the total energy transfer rate can be evaluated via $P=\sum_{\lambda,\lambda'}P_{\lambda\lambda'}$, where $\lambda=+1$ for conduction band and $\lambda=-1$ for valence band, $P_{\lambda\lambda'}=4h\nu\sum_{\mathbf{k}',\mathbf{k}}f_\lambda(\mathbf{k})[1-f_{\lambda'}(\mathbf{k}')]W_{\lambda\lambda'}(\mathbf{k},\mathbf{k}')$ is the energy transfer rate induced by different transition channels, $W_{\lambda\lambda'}(\mathbf{k},\mathbf{k}')$ is the electronic transition rate obtained from Fermi's golden rule, and $f_\lambda(\mathbf{k})\simeq f_\lambda[E_\lambda(\mathbf{k})]$ is the Fermi–Dirac distribution function for carriers in graphene. For a relatively weak radiation field, the optical conductivity can be calculated through $\sigma(\nu)=2P/F_0^2=\sum_{\lambda,\lambda'}\sigma_{\lambda\lambda'}(\nu)$. Furthermore, the optical transmission coefficient for an air/graphene/dielectric-wafer system can be evaluated via [25]

$$T^i(\nu)=\sqrt{\frac{\epsilon_2^i}{\epsilon_1}}\frac{4(\epsilon_1\epsilon_0)^2}{|[(\epsilon_1\epsilon_2^i)^{1/2}+\epsilon_1]\epsilon_0+\sqrt{\epsilon_1}\sigma^i(\nu)/c|^2}, \tag{1}$$

where $\sigma^i(\nu)$ is the optical conductivity for an i-layer graphene system at a radiation frequency ν, $\epsilon_1=1$ and $\epsilon_2^i=\epsilon_\infty^i$ are the dielectric constant of free space and the effective high-frequency dielectric constant of the substrate for different systems, respectively, and c is the speed of light in vacuum.

2.1. Monolayer graphene

The massless Dirac–Weyl quasiparticles of monolayer graphene for a carrier (an electron or a hole) in the monolayer graphene in the π-bands near the K-point can be described by a $\mathbf{k}\cdot\mathbf{p}$ Hamiltonian

$$H_0^{\mathrm{m}}=\begin{pmatrix}0 & \hbar v_0 k_-\\ \hbar v_0 k_+ & 0\end{pmatrix}, \tag{2}$$

where $k_\pm=k_x\pm ik_y=ke^{\pm i\phi}$ with $v_0=10^6$ m/s being the Fermi velocity, $\mathbf{k}=(k_x,k_y)$ is the wavevector for a carrier, and ϕ is the angle between $\mathbf{k}$ and the x-axis. The eigenfunction and the energy eigenvalue are given by $\psi_{\lambda\mathbf{k}}^{\mathrm{m}}(\mathbf{r})=2^{1/2}[e^{-i\phi},\lambda]e^{i\mathbf{k}\cdot\mathbf{r}}$ and $E_\lambda^{\mathrm{m}}(\mathbf{k})=\lambda\hbar v_0 k$, respectively, where $\lambda=+1$ for electron and $\lambda=-1$ for hole. Here, the eigenfunction is in a form of row matrix. In the presence of a weak light field applied perpendicular to the graphene sheet and polarized along the x-direction, the steady-state electronic transition rate induced by direct carrier–photon interaction can be obtained by using Fermi's golden rule, which reads

$$W_{\lambda\lambda'}^{\mathrm{m}}(\mathbf{k},\mathbf{k}')=\frac{2\pi}{\hbar}\left(\frac{eF_0v_0}{4\pi\nu}\right)^2\frac{1+\lambda\lambda'\cos(2\phi)}{2}\times\delta_{\mathbf{k}',\mathbf{k}}\delta[E_{\lambda'}^{\mathrm{m}}(\mathbf{k}')-E_\lambda^{\mathrm{m}}(\mathbf{k})-h\nu]. \tag{3}$$

It measures the probability for scattering of a carrier from a state $|\mathbf{k},\lambda\rangle$ to a state $|\mathbf{k}',\lambda'\rangle$. After considering the effect of the broadening of the scattering states due to energy relaxation through Poisson Kernel: $\delta(E)\to(E_\tau/\pi)(E^2+E_\tau^2)^{-1}$ to replace the δ function for intraband optical transition and using the identity $\int_0^\infty f(x)\delta[g(x)]\,dx=f(x)/|g'(x)|$ in the case that $g(x)=0$ has only a single root for interband optical transition, we can obtain

$$\sigma_{\lambda\lambda}^{\mathrm{m}}(\nu)=\frac{2\sigma_0v_0^2}{\pi^2\nu}\frac{\tau}{(2\pi\nu\tau)^2+1}\int_0^\infty dk\,kf_\lambda[E_\lambda^{\mathrm{m}}(\mathbf{k})]\times\{1-f_\lambda[E_\lambda^{\mathrm{m}}(\mathbf{k})]\}, \tag{4}$$

for transition within the conduction band and valance band, where τ is the energy relaxation time, $E_\tau=\hbar/\tau$ is the energy broadening of the states, and $\sigma_0=\pi e^2/(2h)$.

For interband transition channels, we have $\sigma_{+-}^{\mathrm{m}}(\nu)\simeq 0$ and

$$\sigma_{-+}^{\mathrm{m}}(\nu)=\sigma_0 f_-(-h\nu/2)[1-f_+(h\nu/2)]. \tag{5}$$

2.2. Bilayer graphene

After including the various interlayer coupling such as the near-neighbor and the next-nearest neighbor interactions, the effective Hamiltonian for a carrier (an electron or a hole) in the bilayer graphene in the π-bands near the K-point can be written as [15]

$$H_0^{\mathrm{b}}=\begin{pmatrix}0 & \hbar^2k_-^2/(2m^*)-\hbar u_3k_+\\ \hbar^2k_+^2/(2m^*)-\hbar u_3k_- & 0\end{pmatrix}, \tag{6}$$

where $m^*=\xi_1/(2u_0^2)$, $u_i=\sqrt{3}a\xi_i/2\hbar$, $p=\hbar k$ and a=2.46 Å. Moreover, we quote $\xi_0=3.16$ eV, $\xi_1=0.39$ eV, $\xi_3=0.315$ eV for typical coupling values [26,27] in bilayer graphene. The corresponding Schodinger equation can be solved analytically and the eigenvalue is given as $E_\lambda^{\mathrm{b}}(\mathbf{k})=\lambda A$, where $A=[h_a^2+h_b^2-2\cos(3\phi)h_ah_b]^{1/2}$,

$h_a = p^2/(2m^*)$, and $h_b = pu_3$. The eigenfunction for a carrier in bilayer graphene is $\psi^{b}_{\lambda\mathbf{k}}(\mathbf{r}) = 2^{-1/2}[(h_a e^{-2i\phi} - h_b e^{i\phi})/A, \lambda]e^{i\mathbf{k}\cdot\mathbf{r}}$, in the form of a row matrix, with $\mathbf{r} = (x, y)$. In the presence of a weak light field applied perpendicular to the bilayer graphene sheet, the carrier–photon interaction Hamiltonian within the usual Coulomb gauge for bilayer graphene becomes

$$H^{b}_{cp}(t) = \frac{eA(t)}{m^*}\begin{pmatrix} 0 & m^*u_3 - \hbar k_- \\ m^*u_3 - \hbar k_+ & 0 \end{pmatrix}. \quad (7)$$

Here, the contribution from the F_0^2 term has been neglected. Then the first-order contribution to the steady-state electronic transition rate induced by carrier–photon interaction via absorption scattering is obtained as

$$W^{b}_{\lambda\lambda'}(\mathbf{k},\mathbf{k}') = \frac{2\pi}{\hbar}\left(\frac{eF_0}{4\pi m^*\nu}\right)^2 \frac{|U^{b}_{\lambda\lambda'}(\mathbf{k})|^2}{4A^2}\delta_{\mathbf{k}',\mathbf{k}} \times \delta[E^{b}_{\lambda'}(\mathbf{k}') - E^{b}_{\lambda}(\mathbf{k}) - h\nu], \quad (8)$$

with $|U^{b}_{\lambda\lambda'}(\mathbf{k})|^2 = |[\lambda'\ (h_a e^{-2i\phi} - h_b e^{i\phi}) + \lambda(h_a e^{2i\phi} - \ h_b e^{-i\phi})]m^*u_3 + \hbar k[\lambda'(h_b e^{2i\phi} - h_a e^{-i\phi}) + \lambda(h_b e^{-2i\phi} - h_a e^{i\phi})]|^2$. After considering the effect of the broadening of the scattering states due to energy relaxation through Poisson Kernel, we have

$$\sigma^{b}_{\lambda\lambda}(\nu) = \frac{4\sigma_0}{\pi^3\nu(m^*)^2}\frac{\tau}{(2\pi\nu\tau)^2+1}\int_0^{\pi} d\phi \int_0^{\infty}\frac{dk\,k}{A^2} \times f_{\lambda}[E^{b}_{\lambda}(\mathbf{k})]\{1 - f_{\lambda}[E^{b}_{\lambda}(\mathbf{k})]\}G^{b}_{\lambda\lambda}(k,\phi), \quad (9)$$

for transition within the conduction band and valance band, where $G^{b}_{\lambda\lambda}(k,\phi) = [m^*u_3(h_a\ \cos\ 2\phi - h_b\ \cos\ \phi) + \hbar k(h_b\ \cos\ 2\phi - h_a\ \cos\ \phi)]^2$.

For interband transition channels, we have $\sigma^{b}_{+\ -}(\nu) \simeq 0$ and

$$\sigma^{b}_{-\ +}(\nu) = \frac{4\sigma_0}{\pi^3\nu(m^*)^2}\int_0^{\pi} d\phi \int_0^{\infty}\frac{dk\,k}{A^2}[1 - f_+(h\nu/2)] \times f_-(-h\nu/2)\frac{\tau G^{b}_{-\ +}(k,\phi)}{4\tau^2(\pi\nu - A/\hbar)^2+1}, \quad (10)$$

where $G^{b}_{-\ +}(k,\phi) = [m^*u_3(-h_a\ \sin\ \ 2\phi - h_b\ \sin\ \phi) + \hbar k(h_b\ \sin\ 2\phi + h_a\ \sin\ \phi)]^2$.

2.3. ABC-stacked trilayer graphene

The effective Hamiltonian for a carrier (an electron or a hole) in low-energy regime in ABC-stacked tri-layer graphene (TLG) in the π-bands near the K-point is [17]

$$H^{t}_{0} = \begin{pmatrix} S_1 & S_0\hbar^3k_-^3 + S_2 \\ S_0\hbar^3k_+^3 + S_2 & S_1 \end{pmatrix}, \quad (11)$$

where $S_0 = 3^{3/2}a^3\gamma_0^3/(8\hbar^3\gamma_1^2)$, $S_1 = \gamma_5 - 3\gamma_0\gamma_4k^2a^2/(2\gamma_1)$, and $S_2 = \gamma_2/2 - 3\gamma_0\gamma_3k^2a^2/(2\gamma_1)$, with the typical hoping parameters [17] $\gamma_0 = 3.16$ eV, $\gamma_1 = 0.502$ eV, $\gamma_2 = -0.0171$ eV, $\gamma_3 = -0.377$ eV, $\gamma_4 = -0.099$ eV, $\gamma_5 = -0.0014$ eV. The corresponding Schodinger equation can be solved analytically and the eigenvalue is given as $E^{t}_{\lambda}(\mathbf{k}) = S_1 + \lambda B$ with $B = [S_0^2\hbar^6k^6 + S_2^2 + 2\ \cos(3\phi)\ S_0S_2\hbar^3k^3]^{1/2}$. The corresponding eigenfunction for a carrier in ABC-stacked TLG is $\psi^{t}_{\lambda\mathbf{k}}(\mathbf{r}) = 2^{1/2}[e^{i\psi}, \lambda]e^{i\mathbf{k}\cdot\mathbf{r}}$, in the form of a row matrix, with $e^{i\psi} = (S_0\hbar^3k^3e^{-3i\phi} + S_2)/B$ and $\mathbf{r} = (x, y)$. The carrier–photon interaction Hamiltonian for a ABC-stacked TLG becomes

$$H^{t}_{cp}(t) = \frac{eA(t)}{\hbar}\begin{pmatrix} Q_1 & Q_2 - 3S_0\hbar^3k_-^2 \\ Q_2 - 3S_0\hbar^3k_+^2 & Q_1 \end{pmatrix}, \quad (12)$$

with $Q_1 = 3\gamma_0\gamma_4a^2k\ \cos\ \phi/\gamma_1$ and $Q_2 = Q_1\gamma_3/\gamma_4$. Here we have ignored the contributions from F_0^2 and F_0^3 terms in case of a weak light field. Then the first-order contribution to the steady-state electronic transition rate induced by carrier–photon interaction via absorption scattering is obtained as

$$W^{t}_{\lambda\lambda'}(\mathbf{k},\mathbf{k}') = \frac{2\pi}{\hbar}\left(\frac{eF_0}{4\pi\nu}\right)^2\frac{|U^{t}_{\lambda\lambda'}(\mathbf{k})|^2}{4B^2}\delta_{\mathbf{k}',\mathbf{k}} \times \delta[E^{t}_{\lambda'}(\mathbf{k}') - E^{t}_{\lambda}(\mathbf{k}) - h\nu], \quad (13)$$

where $|U^{t}_{\lambda\lambda'}(\mathbf{k})|^2 = |-3S_0\hbar^2k^2[\lambda'(S_0\hbar^3k^3e^{-i\phi} + \ S_2e^{2i\phi}) + \lambda(S_0\hbar^3k^3e^{i\phi} + S_2e^{-2i\phi})] + [\lambda'(S_0\hbar^3k^3e^{-3i\phi} + S_2) + \lambda(S_0\hbar^3k^3e^{3i\phi} + S_2)]Q_2/\hbar + (1 + \lambda\lambda')Q_1B/\hbar|^2$. Using Poisson Kernel to replace the δ-function, we have

$$\sigma^{t}_{+\ +}(\nu) = \frac{4\sigma_0}{\pi^3\hbar^2\nu}\frac{\tau}{(2\pi\nu\tau)^2+1}\int_0^{\pi} d\phi \int_0^{\infty}\frac{dk\,k}{B^2}f_+[E^{t}_{+}(\mathbf{k})] \times\{1 - f_+[E^{t}_{+}(\mathbf{k})]\}G^{t}_{+\ +}(k,\phi), \quad (14)$$

for transition within the conduction band with $G^{t}_{+\ +}(k,\phi) = [Q_1B - 3S_0\hbar^3k^2(S_0\hbar^3k^3\ \cos\ \phi + S_2\ \cos\ 2\phi) + (S_0\hbar^3k^3\ \cos\ 3\phi + S_2)Q_2]^2$. For transition within the valance band, we obtain

$$\sigma^{t}_{-\ -}(\nu) = \frac{4\sigma_0}{\pi^3\hbar^2\nu}\frac{\tau}{(2\pi\nu\tau)^2+1}\int_0^{\pi} d\phi \int_0^{\infty}\frac{dk\,k}{B^2}f_-[E^{t}_{-}(\mathbf{k})] \times\{1 - f_-[E^{t}_{-}(\mathbf{k})]\}G^{t}_{-\ -}(k,\phi), \quad (15)$$

with $G^{t}_{-\ -}(k,\phi) = [3S_0\hbar^3k^2(S_0\hbar^3k^3\ \cos\ \phi + S_2\ \cos\ 2\phi) - (S_0\hbar^3k^3\ \cos\ 3\phi + S_2)Q_2 + Q_1B]^2$.

For interband transition channels, we have $\sigma^{t}_{+\ -}(\nu) \simeq 0$ and

$$\sigma^{t}_{-\ +}(\nu) = \frac{2\sigma_0\tau}{\pi^2\hbar^2\nu}\int_0^{\pi} d\phi \int_0^{\infty}\frac{dk\,k}{B^2}e^{-|\tau(2\pi\nu - 2B/\hbar)|} \times f_-[E^{t}_{-}(\mathbf{k})]\{1 - f_+[E^{t}_{+}(\mathbf{k})]\}G^{t}_{-\ +}(k,\phi), \quad (16)$$

where $G^{t}_{-\ +}(k,\phi) = [3S_0\hbar^3k^2(S_0\hbar^3k^3\ \sin\ \phi - S_2\ \sin\ 2\phi) - S_0Q_2\hbar^3k^3\ \sin\ 3\phi]^2$ and we have taken an approximation $\delta(E) \to e^{-|E|/E_\tau}/(2E_\tau)$ to replace the δ-function.

2.4. AB-stacked multilayer graphene

For AB-stacked N-layer graphene with $N \geq 3$, the electronic Hamiltonian can be approximately decomposed into subsystems equivalent to monolayer or bilayer graphene and the total optical conductivity can be regarded as a summation over each subsystems [18,26,27]. The Hamiltonian of odd-layered graphene is composed of one monolayer-type and $(N-1)/2$ bilayer-type subbands, while that of even-layered graphene is only composed of $N/2$ bilayers [28]. When we focus mainly on the optical response to long wavelength radiation field, the reduced effective low-energy Hamiltonian for mono- and bi- layer subsystems can be considered as [28,29]

$$H^{M}_{AB} = \begin{pmatrix} q\eta_2 & v_0\hbar k_- \\ v_0\hbar k_+ & q\eta_5 \end{pmatrix}, \quad (17)$$

and

$$H^{Bj}_{AB} = \begin{pmatrix} \alpha_j\eta_2 & -v_0^2\hbar^2k_-^2/(\mu_j\xi_1) \\ -v_0^2\hbar^2k_+^2/(\mu_j\xi_1) & \beta_j\eta_2 \end{pmatrix}, \quad (18)$$

where $\eta_2 = -0.02$ eV, $\eta_5 = 0.04$ eV, $q = (1-N)/(N+1)$, $u_j = 2\ \cos(\kappa_j)$, $\kappa_j = \pi/2 - j\pi/(2N+2)$ and j denotes the index of bilayer subsystem which ranges as

$$j = \begin{cases} 1, 3, 5, \ldots, N-1, & N = \text{even}, \\ 2, 4, 6, \ldots, N-1, & N = \text{odd}. \end{cases} \quad (19)$$

In addition, we have $\alpha_j = \beta_j = [N\ \cos(2\kappa_j) + 1]/(N+1)$ for even N, $\alpha_j = [(N-1)\ \cos(2\kappa_j) + 2]/(N+1)$ and $\beta_j = \cos(2\kappa_j)$ for odd N [27]. For monolayer subsystem, the corresponding eigenvalue and

eigenfunction can be written as

$$E^{M}_{N\lambda}(\mathbf{k})=\frac{q(\eta_2+\eta_5)}{2}+\lambda\sqrt{\frac{q^2(\eta_2-\eta_5)^2}{4}+v_0^2\hbar^2k^2}, \tag{20}$$

and

$$\psi^{M}_{N\lambda\mathbf{k}}(\mathbf{r})=\mathbb{N}^{M}_{N\lambda}[R^{M}_{N\lambda}e^{-i\phi},1]e^{i\mathbf{k}\cdot\mathbf{r}}, \tag{21}$$

respectively, where $R^{M}_{N\lambda}=v_0\hbar k/(E^{M}_{N\lambda}(\mathbf{k})-q\eta_2)$ and $\mathbb{N}^{M}_{N\lambda}=[1+(R^{M}_{N\lambda})^2]^{-1/2}$. For the bilayer subsystem B_j, the corresponding eigenvalue and eigenfunction are

$$E^{B_j}_{N\lambda}(\mathbf{k})=\frac{\eta_2(\alpha_j+\beta_j)}{2}+\lambda\sqrt{\frac{\eta_2^2(\alpha_j-\beta_j)^2}{4}+v_0^4\hbar^4k^4/\mu_j^2\xi_1^2}, \tag{22}$$

and

$$\psi^{B_j}_{N\lambda\mathbf{k}}(\mathbf{r})=\mathbb{N}^{B_j}_{N\lambda}[R^{B_j}_{N\lambda}e^{-2i\phi},1]e^{i\mathbf{k}\cdot\mathbf{r}}, \tag{23}$$

where $R^{B_j}_{N\lambda}=v_0^2\hbar^2k^2/[\mu_j\xi_1(\alpha_j\eta_2-E^{B_j}_{N\lambda}(\mathbf{k}))]$ and $\mathbb{N}^{B_j}_{N\lambda}=[1+(R^{B_j}_{N\lambda})^2]^{-1/2}$. In the presence of a weak and linearly polarized radiation field, the first-order contribution to the steady-state electronic transition rate induced by carrier–photon interaction via absorption scattering for mono- and bi-layer subsystems is obtained as

$$W^{M}_{N\lambda\lambda'}(\mathbf{k},\mathbf{k}')=\frac{2\pi}{\hbar}\left(\frac{eF_0v_0}{4\pi\nu}\right)^2|U^{M}_{N\lambda\lambda'}(\mathbf{k})|^2\delta_{\mathbf{k}',\mathbf{k}}\times\delta[E^{M}_{N\lambda'}(\mathbf{k}')-E^{M}_{N\lambda}(\mathbf{k})-h\nu], \tag{24}$$

where $|U^{M}_{N\lambda\lambda'}(\mathbf{k})|^2=(\mathbb{N}^{M}_{N\lambda}\mathbb{N}^{M}_{N\lambda'})^2[(R^{M}_{N\lambda})^2+(R^{M}_{N\lambda'})^2+2\cos(2\phi)R^{M}_{N\lambda}R^{M}_{N\lambda'}]$, and

$$W^{B_j}_{N\lambda\lambda'}(\mathbf{k},\mathbf{k}')=\frac{2\pi}{\hbar}\left(\frac{eF_0v_0^2\hbar k}{2\pi\nu\mu_j\xi_1}\right)^2|U^{B_j}_{N\lambda\lambda'}(\mathbf{k})|^2\delta_{\mathbf{k}',\mathbf{k}}\times\delta[E^{B_j}_{N\lambda'}(\mathbf{k}')-E^{B_j}_{N\lambda}(\mathbf{k})-h\nu], \tag{25}$$

where $|U^{B_j}_{N\lambda\lambda'}(\mathbf{k})|^2=(\mathbb{N}^{B_j}_{N\lambda}\mathbb{N}^{B_j}_{N\lambda'})^2[(R^{B_j}_{N\lambda})^2+(R^{B_j}_{N\lambda'})^2+2\cos(2\phi)R^{B_j}_{N\lambda}R^{B_j}_{N\lambda'}]$, respectively.

For odd AB-stacked multilayer, the intraband optical conductivity of monolayer subsystem is

$$\sigma^{M}_{N\lambda\lambda}(\nu)=\frac{8\sigma_0v_0^2}{\pi^2\nu}\frac{\tau}{(2\pi\nu\tau)^2+1}\int_0^\infty dk\,k\Big\{1-f_\lambda[E^{M}_{N\lambda}(\mathbf{k})]\Big\}\times f_\lambda[E^{M}_{N\lambda}(\mathbf{k})](\mathbb{N}^{M}_{N\lambda})^4(R^{M}_{N\lambda})^2, \tag{26}$$

within the conduction band and valance band. For interband transition channels, we have $\sigma^{M}_{N+-}(\nu)\simeq 0$ and

$$\sigma^{M}_{N-+}(\nu)=2\sigma_0(\mathbb{N}^{M}_{N-}\mathbb{N}^{M}_{N+})^2[(R^{M}_{N-})^2+(R^{M}_{N+})^2]f_-[E^{M}_{N-}(\mathbf{k})]\times\{1-f_+[E^{M}_{N+}(\mathbf{k})]\}, \tag{27}$$

where $k=[h^2\nu^2-q^2(\eta_2-\eta_5)^2]^{1/2}/(2v_0\hbar)$ for an incident radiation frequency ν in monolayer subsystem.

As for the B_j subsystem in AB-stacked multilayer graphene, we have

$$\sigma^{B_j}_{N\lambda\lambda}(\nu)=\frac{32\sigma_0v_0^4\hbar^2}{\pi^2\nu\mu_j^2\xi_1^2}\frac{\tau}{(2\pi\nu\tau)^2+1}\int_0^\infty dk\,k^3f_\lambda[E^{B_j}_{N\lambda}(\mathbf{k})]\times\{1-f_\lambda[E^{B_j}_{N\lambda}(\mathbf{k})]\}(\mathbb{N}^{B_j}_{N\lambda})^4(R^{B_j}_{N\lambda})^2, \tag{28}$$

for intraband transitions within the conduction band and valance band. For interband transition channels, we have $\sigma^{B_j}_{N+-}(\nu)\simeq 0$ and

$$\sigma^{B_j}_{N-+}(\nu)=4\sigma_0(\mathbb{N}^{B_j}_{N-}\mathbb{N}^{B_j}_{N+})^2[(R^{B_j}_{N-})^2+(R^{B_j}_{N+})^2]f_-[E^{B_j}_{N-}(\mathbf{k})]\times\{1-f_+[E^{B_j}_{N+}(\mathbf{k})]\}, \tag{29}$$

where $k=\{[h^2\nu^2-\eta_2^2(\alpha_i-\beta_i)^2]\mu_j^2\xi_1^2\}^{1/4}/(2^{1/2}v_0\hbar)$ for an incident radiation frequency ν in the B_j bilayer subsystem.

After combining the contributions from each subsystem, the total optical conductivity for an N-layer AB-stacked graphene becomes

$$\sigma^{AB}_{N}(\nu)=\delta_{N,\mathrm{odd}}\sum_{\lambda,\lambda'}\sigma^{M}_{N\lambda\lambda'}(\nu)+\sum_j\sum_{\lambda,\lambda'}\sigma^{B_j}_{N\lambda\lambda'}(\nu). \tag{30}$$

2.5. ABC-stacked multilayer graphene

The ABC-stacked N-layer graphene with $N\geq 3$ constitutes a physical realization of a chiral two-dimensional electron gas (2DEG) with effective low-energy Hamiltonian as [17,29]

$$H^{N}_{ABC}=\frac{v_0^N}{\gamma_1^{N-1}}\begin{pmatrix}0&(\hbar k_-)^N\\(\hbar k_+)^N&0\end{pmatrix}. \tag{31}$$

The corresponding eigenvalue and eigenfunction for an ABC-stacked N-layer graphene with a chirality $J=N$ can be written as $E^{J}_{\lambda}(\mathbf{k})=\lambda(v_0\hbar k)^N/\gamma_1^{N-1}$ and $\psi^{J}_{\lambda\mathbf{k}}(\mathbf{r})=2^{1/2}[\lambda,e^{iN\phi}]e^{i\mathbf{k}\cdot\mathbf{r}}$, respectively. In the presence of a linearly polarized light field, the first-order contribution to the steady-state electronic transition rate induced by carrier–photon interaction via absorption scattering is obtained as

$$W^{J}_{\lambda\lambda'}(\mathbf{k},\mathbf{k}')=\frac{2\pi}{\hbar}\left(\frac{eF_0Nv_0^N(\hbar k)^{N-1}}{4\pi\nu\gamma_1^{N-1}}\right)^2\frac{1+\lambda\lambda'\cos(2\phi)}{2}\times\delta_{\mathbf{k}',\mathbf{k}}\delta[E^{J}_{\lambda'}(\mathbf{k}')-E^{J}_{\lambda}(\mathbf{k})-h\nu]. \tag{32}$$

Following the same theoretical approach for calculating the optical conductance, for ABC-stacked N-layer graphene we have

$$\sigma^{J}_{\lambda\lambda}(\nu)=\frac{2\sigma_0N^2v_0^{2N}\hbar^{2N-2}}{\pi^2\nu\gamma_1^{2N-2}}\frac{\tau}{(2\pi\nu\tau)^2+1}\int_0^\infty dk\,k^{2N-1}\times f_\lambda[E^{J}_{\lambda}(\mathbf{k})]\{1-f_\lambda[E^{J}_{\lambda}(\mathbf{k})]\}, \tag{33}$$

for intraband transitions within the conduction band and valance band. For interband transition channels, we have $\sigma^{J}_{+-}(\nu)\simeq 0$ and

$$\sigma^{J}_{-+}(\nu)=N\sigma_0f_-(-h\nu/2)[1-f_+(h\nu/2)]. \tag{34}$$

3. Results and discussions

In this study, we consider that the conducting carriers in a graphene system are electrons in the absence of the light radiation. The dark electron density is n_0. In the presence of the radiation field, the total electron density becomes $n_e=n_0+\Delta n_e$, where Δn_e is the density of photoexcited electrons, and the hole density is $n_h=\Delta n_e$ due to the law of charge number conservation.

The chemical potential μ^i_λ for electrons and holes in mono-, bi-, and ABC-stacked multi-layer graphene can be determined, respectively, through $n^i_e=g\sum_{\mathbf{k}}f_+[E^i_+(\mathbf{k})]$ and $n^i_h=g\sum_{\mathbf{k}}\{1-f_-[E^i_-(\mathbf{k})]\}$, where $g=4$ counts for spin and valley degeneracy. For AB-stacked multi-layer graphene, the chemical potential for electrons and holes are determined through $n^N_e=g\sum_{\mathbf{k}}\{f_+[E^{M}_{N+}(\mathbf{k})]\delta_{N,\mathrm{odd}}+\sum_j f_+[E^{B_j}_{N+}(\mathbf{k})]\}$ and $n^N_h=g\sum_{\mathbf{k}}\{\{1-f_-[E^{M}_{N-}(\mathbf{k})]\}\delta_{N,\mathrm{odd}}+\sum_j\{1-f_-[E^{B_j}_{N-}(\mathbf{k})]\}\}$, respectively. For the calculation of optical transmittance, we take $\epsilon_2^{\mathrm{m}}=1.2$, $\epsilon_2^{\mathrm{b}}=1.3$ and $\epsilon_2^{\mathrm{t}}=1.5$ for mono-, bi- and ABC-stacked tri- layer graphene system, respectively, where the effect of the dielectric constant mismatch between graphene film and the substrate layer has been taken into account [30]. Furthermore, the energy relaxation time for a high-density graphene device [31] is found to be about $\tau\sim 1$ ps. Thus, we take this value for numerical calculations.

In Fig. 1, we show the contributions from different electronic transition channels to the optical conductance for the fixed electron density n^i_e and hole density n^i_h at a temperature $T=300$ K for mono-, bi-, and ABC-stacked tri-layer graphene systems. We can see the following features. (i) In three graphene systems, the optical absorption via inter-band transition from

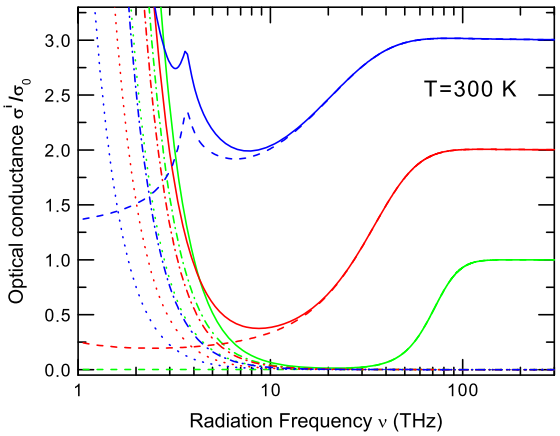

Fig. 1. Contributions from different transition channels to optical conductance at a temperature $T=300$ K for carrier densities $n_e=1.5\times10^{12}$ cm^{-2} and $n_h=5\times10^{11}$ cm^{-2}. The results obtained from mono-, bi- and ABC-stacked tri-layer graphene are show in green, red and blue curves, respectively. Here, σ^i_{++} (dash dot curve), σ^i_{--} (dot curve) and σ^i_{-+} (dash curve) are optical conductance induced by intra-band transitions within the conduction band, within the valence band and by inter-band transition from valence band to conduction band, respectively. The solid curve is the total optical conductance and $\sigma_0=\pi e^2/(2h)$. (For interpretation of the references to color in this figure caption, the reader is referred to the web version of this article.)

valence band to conduction band gives the main contributions in the frequency regime $\nu>20$ THz, whereas the intraband transitions give rise to optical absorption in lower frequency regime. (ii) For mono-, bi- and ABC-stacked tri-layer graphene systems, the optical conductance in frequency range $\nu>130$ THz, $\nu>100$ THz and $\nu>70$ THz depends very weakly on ν, whereas it depends strongly on the radiation frequency in the regime $\nu<130$ THz, $\nu<100$ THz and $\nu<70$ THz, respectively. As we can see, a small absorption peak appears at a frequency about 3.6 THz in ABC-stacked TLG. This small absorption peak is caused by the asymmetry between conduction band and valence band in ABC-stacked TLG. (iii) We find that the optical conductances in high frequency regime for three graphene systems are universal values with $\sigma_0^{\rm m}=\pi e^2/(2h)$, $\sigma_0^{\rm b}=\pi e^2/h$ and $\sigma_0^{\rm t}=3\pi e^2/(2h)$. This confirms that the universal optical conductance per graphene layer is $\pi e^2/(2h)$. (iv) Importantly, we can observe absorption windows in the 1–100 THz frequency range for three graphene systems. These absorption windows are induced by the completing absorption channels with different energies due to inter- and intra-band transitions, as shown in Fig. 1. (v) A red-shift and a narrower and taller absorption window can be observed with increasing number of graphene layers.

The optical conductance and corresponding light transmittance of three graphene systems are shown in Fig. 2 as a function of radiation frequency at fixed carrier densities for different temperatures. As can be seen, $\sigma^i(\nu)$ and $\mathrm{T}^i(\nu)$ depend very little on ν in high frequency regime and they do not vary with temperature. These features are in line with experimental findings for monolayer graphene [22]. The optical absorption window can be observed in far infrared to THz frequency regime where both $\sigma^i(\nu)$ and $\mathrm{T}^i(\nu)$ depend sensitively on temperature. This is in line with the experimental result for mono- [20] and bi-layer [33] graphene systems. We know that the chemical potential for electrons/holes in an electronic system decreases/increases with increasing temperature at a fixed electron/hole density. As a result, due to the Moss–Burstein effect [32], the edge of the optical absorption window shifts to higher energy regime with increasing temperature, as shown in Fig. 2. For monolayer graphene, the width of the optical absorption window decreases with increasing temperature. In bilayer graphene and ABC-stacked TLG systems,

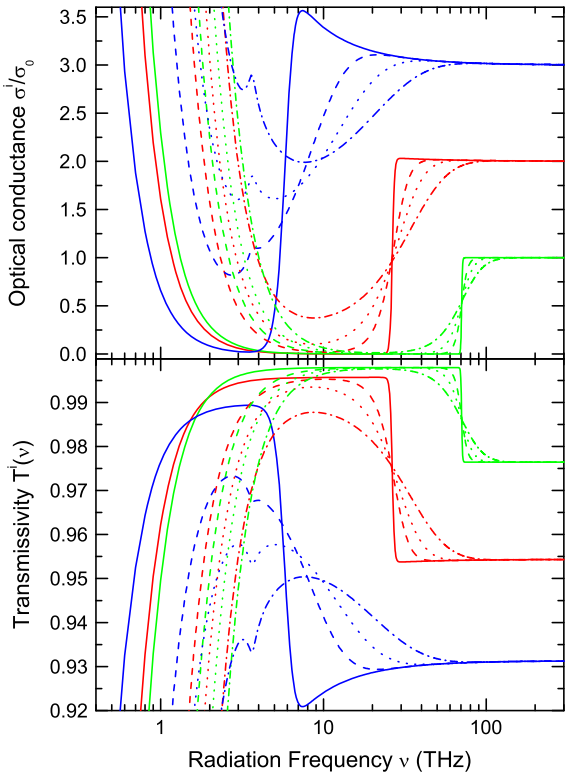

Fig. 2. The optical conductance (upper panel) and light transmittance (lower panel) as a function of radiation frequency ν at the fixed carrier densities $n_e=1.5\times10^{12}$ cm^{-2} and $n_h=5\times10^{11}$ cm^{-2} for different temperatures $T=10$ K (solid curve), 77 K (dashed curve), 150 K (dotted curve), and 300 K (dotted-dashed curve). The results obtained from mono-, bi- and ABC-stacked tri-layer graphene systems are show in green, red and blue curve, respectively. (For interpretation of the references to color in this figure caption, the reader is referred to the web version of this article.)

the hight and width of the optical absorption window decrease with increasing temperature. A wider and deeper optical absorption window and a sharper cutoff of the optical absorption at the window edges can be observed at lower temperatures, in line with experimental finding for monolayer graphene system [20]. The position of the small absorption peak at the frequency about 3.6 THz in ABC-stacked TLG does not change with varying temperature and the strength of this peak becomes weaker with increasing temperature.

The optical conductance and corresponding transmittance of three graphene systems are plotted in Fig. 3 as a function of the radiation frequency at a temperature $T=300$ K and a fixed hole density n_h for different electron densities n_e. For a graphene system placed on a dielectric wafer, applying a positive (negative) gate voltage can pull the electrons (holes) out from the dielectric wafer and inject them into the graphene layer. Then, the electron density in the graphene layer can be varied by the gate voltage [36]. The influence of applying the gate voltage on electronic properties of graphene systems has been investigated theoretically [34,35]. From Fig. 3, we find that in high-frequency regime, the optical conductance does not change with ν and depends very little on electron density in three graphene systems. The absorption windows can be observed in the frequency range 2–150 THz. The small absorption peak at about 3.6 THz in ABC-stacked TLG does not depend on electron density and the strength of it becomes weaker with increasing n_e. Normally, the chemical potential for electrons in the conduction band increases with electron density. Thus, the optical absorption window shifts to higher energy regime with increasing electron density, as shown in Fig. 3. We can see that the height of the absorption window for

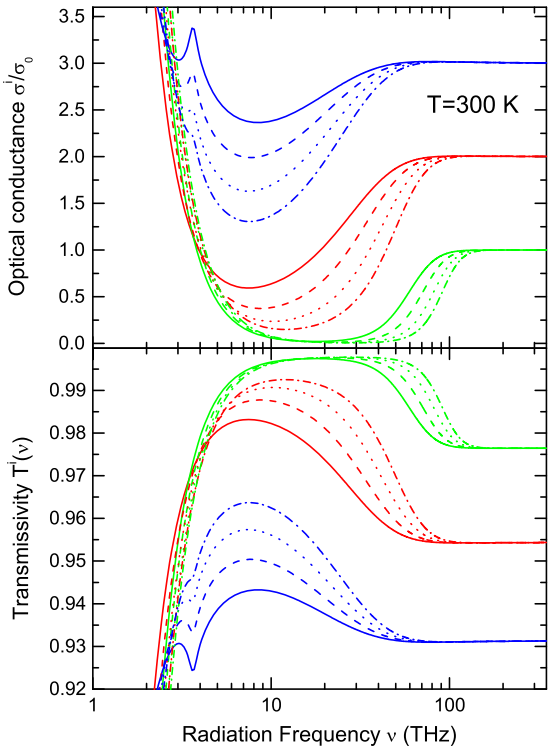

Fig. 3. Optical conductance (upper panel) and transmittance (lower panel) as a function of radiation frequency ν at a temperature $T=300$ K and a fixed hole density $n_h=5\times10^{11}$ cm^{-2} for different electron densities $n_e=1\times10^{12}$ cm^{-2} (solid curve), $n_e=1.5\times10^{12}$ cm^{-2} (dashed curve), $n_e=2\times10^{12}$ cm^{-2} (dotted curve), and $n_e=2.5\times10^{12}$ cm^{-2} (dotted-dashed curve). The results obtained from mono-, bi- and ABC-stacked tri-layer systems are show in green, red and blue curve, respectively. (For interpretation of the references to color in this figure caption, the reader is referred to the web version of this article.)

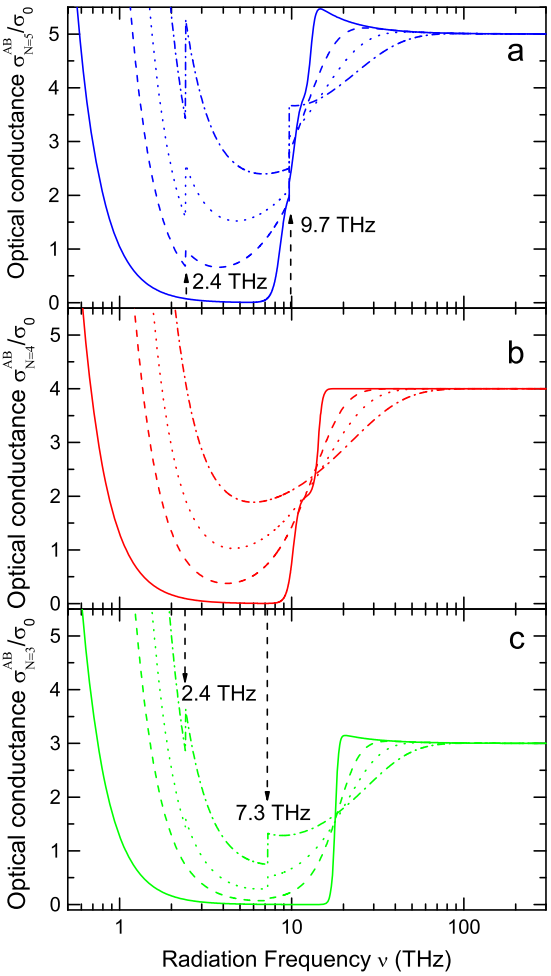

Fig. 4. The optical conductance of AB-stacked graphene multilayer as a function of radiation frequency ν at the fixed carrier densities $n_e=1.5\times10^{12}$ cm^{-2} and $n_h=5\times10^{11}$ cm^{-2} for different temperatures $T=10$ K (solid curve), 77 K (dashed curve), 150 K (dotted curve), and 300 K (dotted-dashed curve). The results are shown for the AB-stacked penta-layer (a, blue curve), tetra-layer (b, red curve), and tri-layer graphene (c, green curve). (For interpretation of the references to color in this figure caption, the reader is referred to the web version of this article.)

different graphene systems increases with electron density and a sharper cutoff of the optical absorption at the window edges can be observed for larger electron density. These results suggest that the width and height of the absorption window in mono-, bi- and ABC-stacked tri-layer graphene systems can be tuned by varying electron density in graphene system through applying a gate voltage.

The optical conductance of AB-stacked multi-layer graphene systems is shown in Fig. 4 as a function of radiation frequency at fixed carrier densities for different temperatures. We can see that the universal optical conductance in visual light regime is contributed by the effective low-energy subsystems with the contribution $\pi e^2/(2h)$ per layer in AB-stacked graphene multilayer. The infrared to THz optical absorption windows can be observed in tri-, tetra- and penta-layer AB-stacked graphene. At lower temperature, a wider and deeper optical absorption window can be achieved and the optical absorption window red-shifts with increasing the layers of graphene sheet. The absorption window also has a red-shift with decreasing temperature. In Fig. 4(a) and (c), we can observe two absorption edges in AB-stacked penta- and tri-layer graphene. These absorption edges are caused by the mini-gaps in AB-stacked multilayer graphene with an odd layer number. In Fig. 4(b), there is no absorption edge because the subsystems in even number AB-stacked mutilayer graphene is gapless. These features can be explained with the help of Eqs. (20) and (22). AB-stacked tri-layer graphene has two mini-gaps with $E^3_{g1}=0.03$ eV and $E^3_{g2}=0.01$ eV which correspond to two absorption edges at 7.3 THz and 2.4 THz, respectively. For AB-stacked penta-layer graphene, there are three mini-gaps with $E^5_{g1}=0.04$ eV, $E^5_{g2}=0.01$ eV and $E^5_{g3}=3.33$ meV. The first two mini-gaps result in two absorption edges at 9.7 THz and 2.4 THz. In the low-frequency regime $\nu<1$ THz, the contribution from interband transition is so weak that we cannot observe the third absorption edge in Fig. 4(a). We also find that the height of the absorption edges increases with increasing temperature. In addition, it should be noted that the band gap absorption edges differ a lot from the absorption window edges which are induced by electronic transition around the Fermi-level. From Fig. 4, we can see that the absorption edges in AB-stacked multilayer graphene are within the window area of the absorption window. In a recent work, Hao [18] calculated the optical conductivity in AB-stacked multilayer graphene in full optical spectrum. It should be noted that Ref. [18] studied the optical conductivity through the full band Hamiltonian and reported how the layer number affects the number of near-infrared and ultraviolet absorption peaks. In Ref. [18], the near-infrared absorption peaks are induced by the optical transitions from the lower energy subsystems to the higher energy subsystems near the K point and the ultraviolet absorption peaks are associated with the Van Hove singularities at M point. In the present study, we employ the effective low-energy model to study the optical response to the radiation field, with which the infrared to THz optical properties can be examined. Additionally, we have demonstrated that the universal optical conductance in visual regime in AB-stacked multilayer graphene is induced only by the

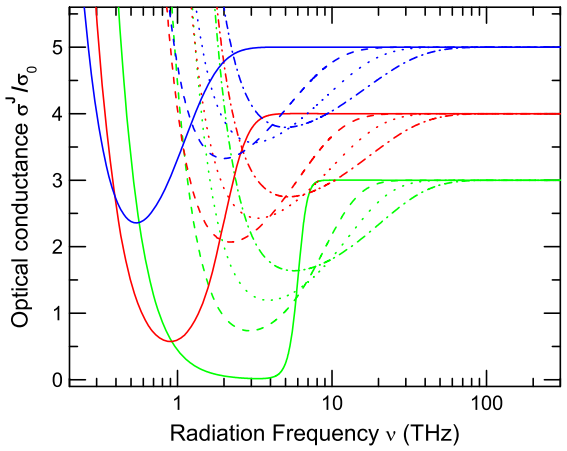

Fig. 5. The optical conductance of ABC-stacked graphene multilayer as a function of radiation frequency ν at the fixed carrier densities $n_e = 1.5 \times 10^{12}$ cm^{-2} and $n_h = 5 \times 10^{11}$ cm^{-2} for different temperatures $T = 10$ K (solid curve), 77 K (dashed curve), 150 K (dotted curve), and 300 K (dotted-dashed curve). The results are shown for graphene sheet with 3 (green curves), 4 (red curves), and 5 (blue curves) carbon layers, respectively. (For interpretation of the references to color in this figure caption, the reader is referred to the web version of this article.)

effective low energy subsystems. We find that the layer number of the graphene sheet can affect effectively the absorption windows in AB-stacked graphene multilayer.

The optical absorption spectrum for ABC-stacked multilayer graphene systems are shown in Fig. 5 at the fixed carrier densities for different temperatures. The universal optical conductance is $N\pi e^2/(2h)$ for a ABC-stacked N-layer graphene in high frequency regime. There also exists the optical absorption window at low frequency regime in ABC-stacked multilayer graphene. In Fig. 5, we can see that the absorption window red-shifts to low frequency regime with increasing layer number N or decreasing temperature. Meanwhile, the width and depth of the absorption window decreases with increasing graphene layer number N. Moreover, we note that the absorption window in Fig. 5 shows some different features from those in Fig. 4. (i) Unlike the abundant low energy subsystems in AB-stacked multilayer graphene, ABC-stacked multilayer graphene only has one effective low energy subsystem. Thus, the relatively richer structure of the absorption window can be observed in AB-stacked multilayer graphene than ABC-stacked systems. (ii) ABC-stacked multilayer graphene has a narrower absorption window than that in AB-stacked multilayer graphene with the same layer number. (iii) The depth of the optical absorption window in AB-stacked multilayer graphene is deeper than that in ABC-stacked graphene multilayer. (iv) At low temperatures, the shift of the absorption window tuned by temperature and layer number of graphene sheet is more obvious in ABC-stacked multilayer. These results suggest that the stacking order in multilayer graphene systems also plays an important role in determining the optoelectrical properties in infrared to THz bandwidth.

The results obtained from this study show that the strength of optical absorption increases with increasing number of graphene layers in whole optical spectrum. In infrared to THz regime, optical absorption windows can be seen in mono- and multi-layer graphene systems with AB- and ABC-stacking. The red-shift of the optical absorption window can be observed with increasing number of graphene layers. The main physical reason behind these interesting features is that the mono- and multi-layer graphene systems have different electronic energy spectra. This can result in different density-of-states for optical transition scattering required by momentum and energy conservation laws in different graphene systems. These theoretical findings suggest that the optoelectronic properties of graphene systems can be tuned and modified not only by varying temperature and carrier density but also by choosing graphene sheet with different layers and with different stacking orders.

4. Conclusions

In this study, we have developed a simple theoretical approach to study optoelectronic properties of mono- and multi-layer graphene systems with AB- and ABC-stacking. We have examined the dependence of optical absorption/transmission on temperature, electron density, stacking type and number of graphene layers in air/graphene/dielectric-wafer systems. It has been demonstrated theoretically that the optical conductance is universal values $\sigma_0^N = N\pi e^2/(2h)$ for N-layer graphene systems in the high frequency regime and they depend very little on temperature, electron density and stacking type. This finding confirms that the optical conductance per graphene layer is given by a universal value $\sigma_0 = \pi e^2/(2h)$ in the high frequency regime. The corresponding optical transmission coefficients in high frequency regime are about 97.7%, 95.4% and 93.1% for mono-, bi- and ABC-stacked tri-layer graphene, respectively, in agreement with the experimental data [22]. We have shown that there exist optical absorption windows in the radiation frequency range 0.2–150 THz for mono- and multi-layer graphene systems with AB- and ABC stacking. The Drude-like optical conductance and the corresponding high transmittance windows in infrared to THz regime have been verified experimentally [11,19]. The optical absorption windows in few layer graphene systems are induced by different transition energies required for inter- and intra-band transition channels. The depth and width of such absorption windows depend sensitively on the temperature, electron density, stacking type and the number of graphene layers, especially at lower frequency edge. There is a small absorption peak at the frequency about 3.6 THz in ABC-stacked tri-layer graphene system which does not change the position with varying temperature and electron density but the strength of it decreases with decreasing temperature and/or increasing electron density. For AB-stacked multi-layer graphene with an odd layer number, there exists mini-gap induced absorption edges. The number and the position of the absorption edges depend on the graphene layers' number N. They depend weakly on temperature but the strength of them increase with increasing temperature. At lower temperature and/or larger electron density, we can observe the prominent cutoff of the optical absorption at the window edges in graphene systems. The optical absorption window in AB-stacked N-layer graphene is wider and deeper than that in ABC-stacked multilayer graphene. The optical absorption window red-shifts and the width of the absorption window decreases with an increase in the number of graphene layers. These theoretical results indicate that mono- and multi-layer graphene with AB- and ABC-stacking have some unique features in infrared to THz bandwidth, which can be utilized for application as infrared or THz optoelectronic devices.

Acknowledgments

This work was supported by the Ministry of Science and Technology of China (Grant no. 2011YQ130018), Department of Science and Technology of Yunnan Province, and by the Chinese Academy of Sciences.

References

[1] K.S. Novoselov, A.K. Geim, S.V. Morozov, et al., Science 306 (2004) 666.
[2] H. Hogan, Photon. Spectra 42 (2008) 19.

[3] Weiwei Cai, Yanwu Zhu, Xuesong Li, Richard D. Piner, R.S. Ruoff, Appl. Phys. Lett. 95 (2009) 123115.
[4] B. Sensale-Rodriguez, T. Fang, R. Yan, et al., Appl. Phys. Lett. 99 (2011) 113104.
[5] B. Sensale-Rodriguez, R. Yan, M. Zhu, D. Jena, L. Liu, H.G. Xing, Appl. Phys. Lett. 101 (2012) 261115.
[6] C.-C. Lee, S. Suzuki, W. Xie, T.R. Schibli, Opt. Express 20 (2012) 5264.
[7] J. Park, Y.H. Ahn, C. Ruiz-Vargas, Nano Lett. 9 (2009) 1742.
[8] E.J.H. Lee, K. Balasubramanian, R.T. Weitz, M. Burghard, K. Kern, Nat. Nanotechnol. 3 (2008) 486.
[9] T. Mueller, F. Xia, P. Avouris, Nat. Photon. 4 (2010) 297.
[10] G. Konstantatos, M. Badioli, L. Gaudreau, J. Osmond, et al., Nat. Nanotechnol. 7 (2012) 363.
[11] Jason Horng, Chi-Fan Chen, Baisong Geng, Caglar Girit, et al., Phys. Rev. B 83 (2011) 165113.
[12] A.R. Wright, X.G. Xu, J.C. Cao, C. Zhang, Appl. Phys. Lett. 95 (2009) 072101.
[13] Y.S. Ang, S. Sultan, C. Zhang, Appl. Phys. Lett. 97 (2010) 243110.
[14] W. Xu, Y.P. Gong, L.W. Liu, H. Qin, Y.L. Shi, Nanoscale Res. Lett. 6 (2011) 250.
[15] E. McCann, V.I. Fal'ko, Phys. Rev. Lett. 96 (2006) 086805.
[16] F. Guinea, A.H. Castro Neto, N.M.R. Peres, Phys. Rev. B 73 (2006) 245426.
[17] Fan Zhang, Bhagawan Sahu, Hongki Min, A.H. MacDonald, Phys. Rev. B 82 (2010) 035409.
[18] L. Hao, L. Sheng, Solid State Commun. 149 (2009) 1962.
[19] J.M. Dawlaty, S. Shivaraman, J. Strait, et al., Appl. Phys. Lett. 93 (2008) 131905.
[20] A.B. Kuzmenko, E. van Heumen, F. Carbone, D. van der Marel, Phys. Rev. Lett. 100 (2008) 117401.
[21] Z.Q. Li, E.A. Henriksen, Z. Jiang, et al., Nat. Phys. 4 (2008) 532.
[22] R.R. Nair, P. Blake, A.N. Grigonrenko, K.S. Novoselov, T.J. Booth, T. Stauber, N.M. R. Peres, A.K. Geim, Science 320 (2008) 1308.
[23] H.M. Dong, W. Xu, J. Zhang, Y.Z. Yuan, Opt. Commun. 283 (2010) 3695.
[24] W. Xu, H.M. Dong, L.L. Li, J.Q. Yao, P. Vasilopoulos, F.M. Peeters, Phys. Rev. B 82 (2010) 125304.
[25] T. Stauber, N.M.R. Peres, A.K. Geim, Phys. Rev. B 78 (2008) 085432.
[26] M. Koshino, T. Ando, Phys. Rev. B 77 (2008) 115313.
[27] M. Koshino, T. Ando, Solid State Commun. 149 (2009) 1123.
[28] M. Koshino, E. McCann, Phys. Rev. B 83 (2011) 165443.
[29] H. Min, A.H. MacDonald, Prog. Theor. Phys. Suppl. 176 (2008) 227.
[30] H.M. Dong, W. Xu, Z. Zeng, T.C. Lu, F.M. Peeters, Phys. Rev. B 77 (2008) 235402.
[31] D. Sun, Z.-K. Wu, C. Divin, X. Li, C. Berger, et al., Phys. Rev. Lett. 101 (2008) 157402.
[32] E. Burstein, Phys. Rev. 93 (1954) 632.
[33] X. Zou, J. Shang, J. Leaw, Z. Luo, Liyan Luo, et al., Phys. Rev. Lett. 110 (2013) 067401.
[34] A.A. Avetisyan, B. Partoens, F.M. Peeters, Phys. Rev. B 80 (2009) 195401.
[35] E. McCann, Phys. Rev. B 74 (2006) 161403.
[36] F. Wang, Y. Zhang, C. Tian, C. Giri, A. Zettl, M. Crommie, Y. Ron Shen, Science 320 (2008) 206.